PERGAMON

International Journal of Heat and Mass Transfer 45 (2002) 4451–4461

International Journal of HEAT and MASS TRANSFER

www.elsevier.com/locate/ijhmt

Mixing and film cooling in supersonic duct flows

V. Schuchkin [a], M. Osipov [a], W. Shyy [b,*], S. Thakur [b]

[a] Department of Power Engineering, Bauman Moscow State Technical University, 107005, 2nd Baumanskaya Street 5, Moscow, Russia
[b] Department of Aerospace Engineering, Mechanics and Engineering Science, University of Florida, 231 Aerospace Building, P.O. Box 116250, Gainesville, FL 32611, USA

Received 8 March 2002; received in revised form 11 April 2002

Abstract

A study for gas dynamics and heat transfer characteristics is presented for supersonic turbulent flows inside a channel of rectangular cross-section, with film cooling provided by tangential injection of coolant through the porous slots. A Navier–Stokes-based model with both original and non-equilibrium versions of the k–ε two-equation turbulence model, and an integral method have been assessed with experimental measurements to gain insight into the fluid physics, and to assess the current predictive capability for such flows. Navier–Stokes-based computations show that the interaction between the main and film flows leads to mixing and recirculation, with the overall flow and pressure fields reasonably predicted. However, the computed temperature distribution on the adiabatic wall and pressure at the injection points exhibit noticeable differences compared to the experimental measurements. The integral method is shown to be capable of accounting for the wall temperature profile under the given flow condition and geometry. Further development of the film cooling technologies for supersonic flows can benefit from the present coordinated approach utilizing the detailed Navier–Stokes and integral models along with direct experimental evaluations.

1. Introduction

Film cooling by injection through slots is often employed in power generation devices such as combustion chambers and turbines. This topical area has received much attention over the last several decades, e.g., [1–4]. In addition to physical measurements, earlier efforts on the analysis of heat and mass transfer processes of such flows [5–8] have been complemented by computational tools for single and multiple slot film flows [9,10]. However, less attention has been paid to film cooling with injection through the porous slot [11,12], especially under supersonic flow conditions. It is known that tangential slot film-flow injection reduces wall friction downstream of the injection point, except for low injection mass flow rate, under which recirculation occurs [13,14] and changes the near-wall turbulence structure [14,15]. For low-speed subsonic mean-flows the density fluctuations in a mixing layer at a given free-stream Mach number are approximately three times [16,17] as large as those in a boundary layer at the same free-stream Mach number. As the Mach number increases, the skin-friction coefficient in a boundary layer decreases and the spreading rate and turbulence intensity in a mixing layer also decreases [16,17]. Based on the experimental investigation, whose conditions are summarized in Table 1, it is found that a uniform speed distribution, established by tangential injection through porous slots, can reduce the skin friction and mixing losses. This fact makes it possible to reach an appropriate film cooling efficiency even with relatively low mass-flow rates: $j = (\rho u)_{\text{slot}}/(\rho u)_{\text{main}} < 0.3$. In order to understand the physics involved and to develop improved design guidelines for such film cooling techniques, one needs to be able to predict the gas dynamics and heat-transfer characteristics associated with the mean and coolant flow downstream the injection point. A Navier–Stokes-based model with both original and non-equilibrium versions of the k–ε two-equation turbulence models, an integral method, and experimental measurements have been conducted to assess the current

* Corresponding author. Tel.: +1-352-392-0961; fax: +1-352-392-7303.
E-mail address: wei-shyy@ufl.edu (W. Shyy).

0017-9310/02/$ - see front matter © 2002 Published by Elsevier Science Ltd.
PII: S0017-9310(02)00151-5

Nomenclature

j	relative momentum flux
H	specific total enthalpy
h	specific static enthalpy
k	turbulent kinetic energy
n	exponent in velocity power law, $\omega = u/u_\infty = (y/\delta)^n$
Pr	Prandtl number
P	production term in k-equation, $\mu_t\left(\frac{\partial u_i}{\partial x_j}+\frac{\partial u_j}{\partial x_i}\right)\frac{\partial u_i}{\partial x_j}$
p	instantaneous static pressure
q	heat flux vector
Re	Reynolds number
Re_L	identity Reynolds number, $u_\infty\rho_\infty 1/\mu_\infty$
Re_H^{**}	enthalpy thickness based Reynolds number, $u_\infty\rho_\infty\delta_H^{**}/\mu_\infty$
Re_{H0}^{**}	enthalpy thickness based initial Reynolds number at the injection point/the prehistory of the flow, $u_\infty\rho_\infty\delta_{H0}^{**}/\mu_\infty$
St	Stanton number
St_0	Stanton number at standard conditions, on the smooth flat surface
T	temperature
t^+	non-dimensional wall temperature
x, y	spatial coordinates
x_0	effective cooling length
y_n	near-wall control volume height
y_p	distance normal to the wall till the nearest from the wall computational node
y^+	non-dimensional normal to the wall distance, $\rho y u_\tau/\mu$, $u_\tau = \sqrt{\tau_w/\rho_w}$
Θ	film cooling efficiency, $(H_\infty - H_{wall})/(H_\infty - H_{slot})$
Ψ	relative law of heat transfer, St/St_0
$\delta_{i,j}$	Kronecker delta
δ	boundary layer thickness
δ^{**}	momentum layer thickness
δ_H^{**}	enthalpy layer thickness,
ε	rate of dissipation of turbulent kinetic energy
κ	von Karman constant
μ	coefficient of viscosity
ρ	density
τ	shear stress
$\overline{}$	Reynolds (ensemble) average
$\sim$	Favre (mass-weighted average)
$\cup$	normalized computational variables

Subscripts

H	enthalpy based quantity
main	main flow inlet condition
ref	reference quantity
slot	injection condition
t	turbulent quantity
T∞	quantity at the edge of thermal boundary layer
w, wall	wall condition
∞	free-stream condition
1, 2	denote the parameters of the first and second injection slots

Superscripts

$+$	non-dimensional quantity
$**$	momentum, enthalpy thickness based quantity

predictive capability for such flows. The engineering Navier–Stokes model can benefit from the insight gained from the integral and experimental approaches.

2. Problem description and computational model

2.1. Problem description

The present flow configuration involves two effective heat protection methods, namely, the film cooling and porous materials upstream of the injection location. Fig. 1 illustrates the main features of the geometric definition. In the present study, only the interaction of a high-temperature supersonic flow with film cooling out of the porous slots is investigated.

The bottom wall of the rectangular channel has two porous sections, arranged to form two backward-facing steps, which serve as injection slots for the film cooling flows (see Fig. 1). Each porous section has an impermeable layer on the side contacting the main flow and a permeable porous slot on the side normal to the flow. The cooling air, passing through the porous wall sections, is injected into the channel through the porous slots forming a thin layer on the surface of the next section for its heat protection.

The parameters of experimental setup are given in the Table 1. The distribution of temperature on the bottom wall of the channel is obtained experimentally. The static pressure is measured on the channel inlet and outlet sections and at the points of injection, which are marked with arrows on Fig. 1 for clarity.

A Navier–Stokes-based numerical algorithm employing two versions of k–ε turbulence model [19–21] has been conducted at the corresponding to experiment operational conditions, shown in Table 1. Due to the

Table 1
Experimental setup of the flow condition

Nomenclature	Dimensions	Experimental data
Main supersonic flow of combustion gases		
Inlet speed	[m/s]	990
Inlet stagnation pressure	[kPa]	246
Inlet static pressure	[kPa]	94.1
Inlet stagnation temperature	[K]	1773
Inlet Mach number	[m]	1.292
Channel height	–	0.035
Channel width	[m]	0.070
First film-flow inlet, atmosphere air		
First slot	[mm]	2.6
Mass flux	[kg/s]	0.0027
Inlet film-flow temperature	[K]	583
Static pressure behind the slot	[Pa]	94 800
Second film-flow inlet, atmosphere air		
Second slot	[mm]	1.3
Mass flux	[kg/s]	0.004
Inlet film-flow temperature	[K]	528
Static pressure behind the slot	[Pa]	94 900

geometric configuration, the flow can be considered as two-dimensional. The heat and mass-transfer processes on the adiabatic (see Fig. 1) film cooling wall are the focus of this investigation. The experimental measurement of the wall temperature distribution is compared with the numerical as well as a semi-analytical integral method. The pressure distribution in the near-slot regions is also analyzed.

2.2. Governing equations

The Favre-averaged equations governing the fluid flow for mass continuity, momentum and energy transport are given below:

$$\frac{\partial \rho}{\partial t}+\frac{\partial}{\partial x_j}(\rho u_j)=0 \tag{1}$$

$$\frac{\partial}{\partial t}(\rho u_i)+\frac{\partial}{\partial x_j}(\rho u_j u_i)=-\frac{\partial p}{\partial x_i}+\frac{\partial \tau_{ij}}{\partial x_j} \tag{2}$$

$$\begin{aligned}\frac{\partial}{\partial t}(\bar{\rho}\widetilde{H}-\bar{p})+\frac{\partial}{\partial x_j}(\bar{\rho}\widetilde{u_j}\widetilde{H}) &= -\frac{\partial}{\partial x_j}\left[\left(\frac{\mu}{Pr}+\frac{\mu_t}{Pr_t}\right)\frac{\partial \tilde{h}}{\partial x_j}\right] \\ &+\frac{\partial}{\partial x_j}\left[\tilde{u}_j\left\{(\mu+\mu_t)\left(\frac{\partial \tilde{u}_i}{\partial x_j}+\frac{\partial \tilde{u}_j}{\partial x_i}\right)\right.\right. \\ &\left.\left.-\frac{2}{3}(\mu+\mu_t)\frac{\partial \tilde{u}_l}{\partial x_l}\delta_{i,j}\right\}\right]+\frac{\partial}{\partial x_j}\left[\left(\mu+\frac{\mu_t}{\sigma_k}\right)\frac{\partial \tilde{k}}{\partial x_j}\right]\end{aligned} \tag{3}$$

The Bousinesq Eddy-viscosity hypothesis is employed to yield the turbulent shear stresses:

$$\tau_{ij}=(\mu+\mu_t)\left(\frac{\partial u_i}{\partial x_j}+\frac{\partial u_j}{\partial x_i}\right)-\frac{2}{3}(\mu+\mu_t)\frac{\partial u_l}{\partial x_l}\delta_{ij} \tag{4}$$

The original form of the k–ε turbulence model [22] has been applied to represent the Reynolds stresses:

$$\frac{\partial(\rho u_j k)}{\partial x_j}=\frac{\partial}{\partial x_j}\left[\left(\mu+\frac{\mu_t}{\sigma_k}\right)\frac{\partial k}{\partial x_j}\right]+P-\rho\varepsilon \tag{5}$$

$$\frac{\partial(\rho u_j \varepsilon)}{\partial x_j}=\frac{\partial}{\partial x_j}\left[\left(\mu+\frac{\mu_t}{\sigma_\mu}\right)\frac{\partial \varepsilon}{\partial x_j}\right]+C_{\varepsilon 1}\frac{\varepsilon}{k}P-C_{\varepsilon 2}\rho\frac{\varepsilon^2}{k} \tag{6}$$

$$P=\mu_t\left(\frac{\partial u_i}{\partial x_j}+\frac{\partial u_j}{\partial x_i}\right)\frac{\partial u_i}{\partial x_j} \tag{7}$$

$$\mu_t=\rho C_\mu\frac{k^2}{\varepsilon} \tag{8}$$

There are five parameters that need to be determined in the original k–ε two-equation model, namely, the turbulent Prandtl numbers for k and ε (σ_k and σ_ε), two coefficients regulating the magnitude of production and dissipation in the ε-equation ($C_{\varepsilon 1}$ and $C_{\varepsilon 2}$), and the

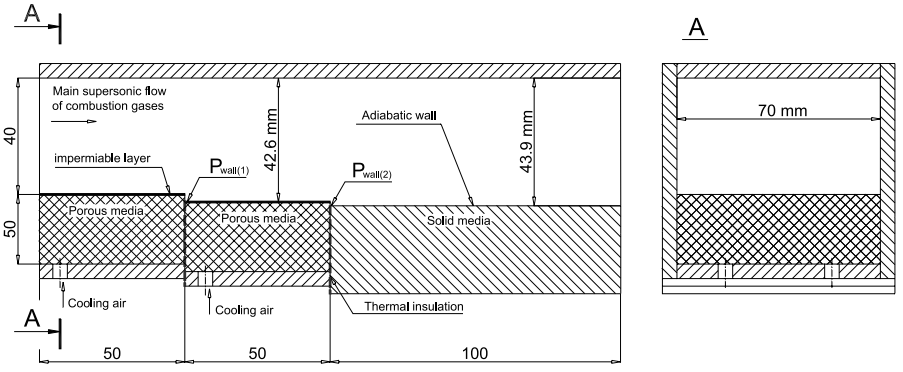

Fig. 1. Schematic two-dimensional side view of experimental channel.

Table 2
Coefficients of the original k–ε model

C_μ	$C_{\varepsilon 1}$	$C_{\varepsilon 2}$	σ_k	σ_ε
0.09	1.44	1.92	1.0	1.3

coefficient regulating the eddy viscosity (C_μ). Coefficients $C_{\varepsilon 1}$, $C_{\varepsilon 2}$ and C_μ are determined largely based on the equilibrium condition, in which case the production and dissipation of k balance each other and convective/diffusive effects are negligible [19]. The constants are summarized in Table 2.

2.3. Numerical technique

A multi-block, finite volume, pressure-based flow solver [19–21] is employed. Diffusion and pressure terms in the momentum equation and the divergence terms in the mass continuity equation are approximated by second-order central difference operators. The second-order upwind [20–22] scheme is adopted to treat the convection terms. The computational domain is treated as two-dimensional.

The Cartesian velocity components are treated as the primary variables, while the contra-variant velocity and pressure fields are updated using a pressure correction equation, which is derived by manipulating the continuity and the momentum equations. The whole process is repeated until the desired convergence is achieved. For detailed discussions, see Refs. [20,23].

2.4. Boundary conditions

Through the series of test-computations the influencing of non-isothermal upstream conditions (porous-cooling walls) on the flow structure and thus temperature distribution along the analyzing adiabatic wall are found to be negligible. Thus all these boundaries are considered as adiabatic. The well-known wall functions for velocity and temperature are employed to provide the wall boundary treatments. Assuming a two-layer structure of the boundary layer, the wall functions have the following forms:

$$\left.\begin{aligned} u^+ &= y^+ \\ u^+ &= \tfrac{1}{\kappa}\log(Ey^+) \end{aligned}\right\} \begin{aligned} &y^+ \leqslant 11.63 \\ &y^+ \geqslant 11.63 \end{aligned}; \qquad \left.\begin{aligned} t^+ &= Pr\, y^+ \\ t^+ &= Pr_t\{u^+ + f(Pr/Pr_t)\} \end{aligned}\right\} \begin{aligned} &y^+ \leqslant 13.2 \\ &y^+ \geqslant 13.2 \end{aligned} \tag{9}$$

where quantity $E = 8.4$ and the von Karman's constant $\kappa = 0.41$. To provide turbulence model closure on the no-slip boundaries, the production and dissipation terms of k-equation are estimated in the near-wall nodes as follows:

$$P = \frac{\tau_{\text{wall}}^2}{\kappa C_\mu^{1/4}\rho y_n k^{1/2}} \ln\left(\frac{2y_p^+}{y_{\text{vis}}^+}\right) \tag{10}$$

$$-\rho\varepsilon = \frac{\rho}{y_n}\int_0^{y_n} \varepsilon\, \mathrm{d}y = \frac{2\mu k}{y_{\text{vis}} y_n} + \frac{C_\mu^{3/4}\rho k^{3/2}}{\kappa y_n}\ln\left(\frac{2y_p^+}{y_{\text{vis}}^+}\right) \quad (\text{if } y^+ < y_{\text{vis}}^+) \quad (\text{if } y^+ > y_{\text{vis}}^+) \tag{11}$$

where y_p^+ is the normalized distance between the wall and the near-wall node; $y_{\text{vis}}^+ = 11.63$ represents the viscous sublayer thickness. In Eq. (10), the magnitude of shear stress value is estimated as follows:

$$\tau_{\text{wall}} = \frac{\mu y^+}{y_p u^+} u \tag{12}$$

At the main inlet of supersonic flow, indicated in Fig. 2, the Mach number of the main flow is 1.29 and the Reynolds number, based on the hydraulic diameter of the channel, is taken as 10^6. Both injected flows are subsonic with injection intensities $j_1 = (\rho u)_{\text{slot1}}/(\rho u)_{\text{main}} = 0.07$ for the first and $j_2 = 0.26$ for the second slot, respectively. The magnitudes of experimentally measured mass fluxes and fluid temperatures, shown in Table 1, are specified as boundary conditions for film-flow inlets. All variables at the channel outlet are estimated based on a linear extrapolation from the interior nodes.

The dimensional variables used in the computation are normalized as follows:

$$\breve{\rho} = \frac{\rho}{\rho_{\text{ref}}} \quad \breve{L} = \frac{L}{L_{\text{ref}}} \quad \breve{U} = \frac{U}{U_{\text{ref}}} \quad \breve{T} = \frac{T}{T_{\text{ref}}} \tag{13}$$

2.5. Main inlet boundary conditions

Consistent with the experimental observations, a turbulent boundary layer exists when the flow enters the main channel (Fig. 1). Different values of boundary layer thickness, at the inlet, are tested to examine their influence on the results of the computation. The mean-velocity profiles are estimated using the power law [5]:

$$\omega = \frac{u}{u_\infty} = \left(\frac{y}{\delta}\right)^n \tag{14}$$

The momentum thickness-based Reynolds number is taken to be in the range $Re^{**} < 10^4 < 10^6$ and $n = 1/7$ [5].

Two computations with different incoming boundary layer thickness (2 and 6.5 mm) have been performed along with a uniform supersonic inlet. Fig. 3(a) compares temperature distributions on the adiabatic wall downstream of the second injection slot. The corresponding mean-velocity initial profiles are presented in Fig. 3(b). The comparison of static pressure downstream of the injection slots is presented in the Table 3.

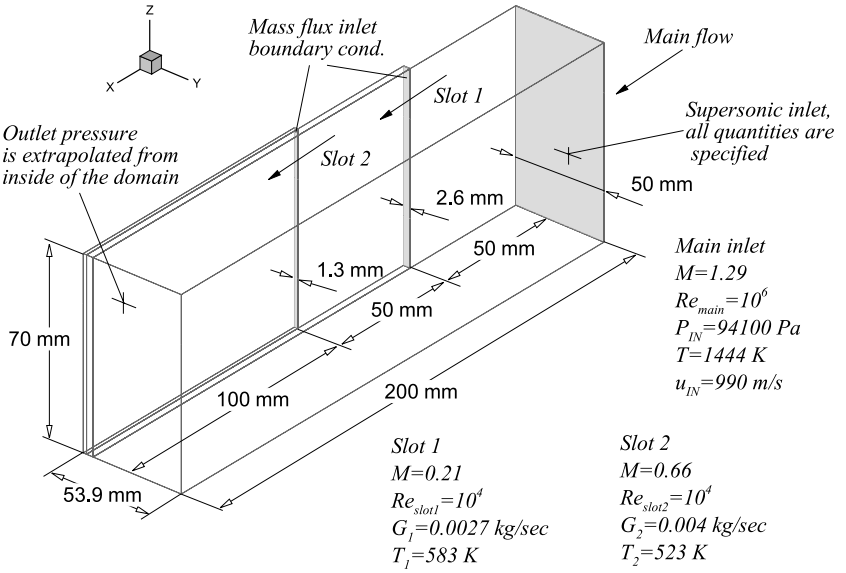

Fig. 2. Boundary conditions. (The Reynolds numbers presented are based on the hydraulic diameters of the inlets.)

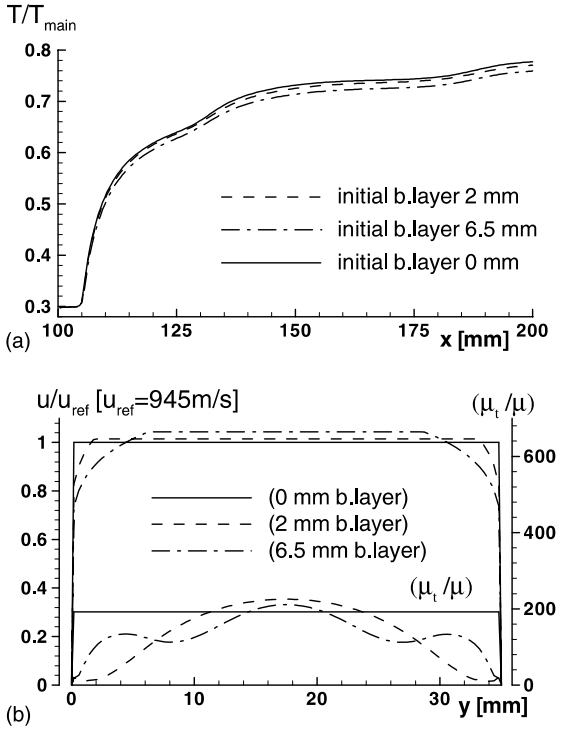

Fig. 3. (a) Temperature distribution along the adiabatic wall/ comparison for different initial conditions; (b) main flow inlet initial-velocity and corresponding effective viscosity profiles.

It is concluded that the incoming boundary layer thickness does not substantially influence the flow structure downstream of the injection slots.

Table 3
Effect of the boundary layer thickness on the predicted wall pressure in the near-slot regions; subscripts 1 and 2 denote the identity of the slot, "*main*"—the main flow inlet condition. (b.l. = boundary layer)

Uniform distribution	2 mm b.l. thickness	6.5 mm b.l. thickness
p_1/p_{main} 0.740	0.764	0.773
p_2/p_{main} 0.828	0.828	0.828

3. Results and discussion

3.1. Mesh distribution and refinement study

Fig. 4 shows the computational domain composed of three grid blocks. The multi-block grid layout with three spatial resolutions, labeled as coarse, medium and fine grids, are shown in Fig. 4. Table 4 lists the dimensions of the different grids employed. Regions A and B in Fig. 4 demonstrate the mesh characteristics in the areas around the first and the second steps.

To illustrate the overall flow structure, the pressure distribution over the computational domain for the fine mesh is presented in Fig. 5(a). Expansion waves at the corners of the steps and compression waves downstream of the steps can be observed, as one would expect in a supersonic flow over backward-facing steps [16]. Fig. 5(b) compares the bottom wall-pressure distributions using coarse, medium and fine grids. It is clearly seen in

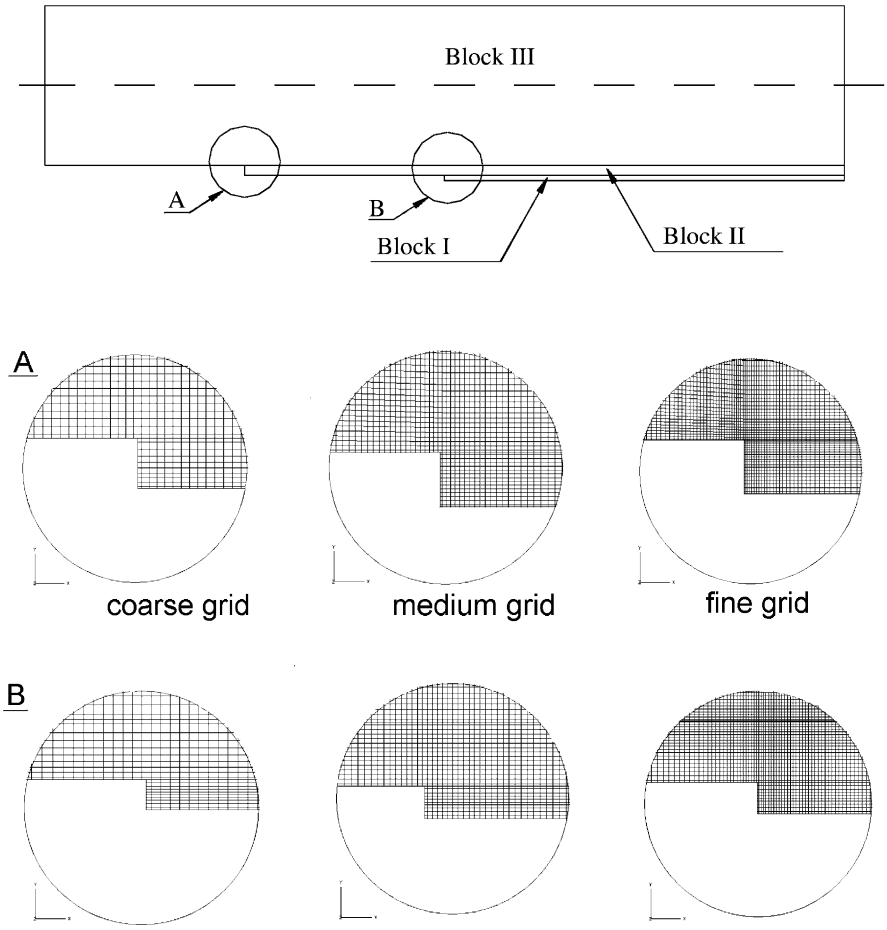

Fig. 4. Mesh characteristics in the near-slot regions, with different grid sizes.

Table 4
Coarse, medium and fine grid nodes quantities

	Coarse grid	Medium grid	Fine grid
Block 1	200×10	220×10	250×10
Block 2	300×10	340×15	450×20
Block 3	400×100	450×100	575×110
Total number of grids	459,000	530,865	747,810

Fig. 5(b) that the fine grid, which contains twice as many grid points as the coarse grid, leads to solutions comparable to those obtained on the coarse grid. The results presented in the rest of the paper are based on the coarse mesh computations.

3.2. Pressure and momentum

The film flow at the first slot has a relatively low intensity ($j_1 = (\rho u)_{\text{slot1}}/(\rho u)_{\text{main}} = 0.07$) and does not significantly influence the streamline pattern (Fig. 6(a)). The only effect of this flow is to shift the recirculation region to a slightly further downstream position.

As can be seen in Fig. 6(a), an expansion wave occurs at the edge of the first step. The pressure in the separated region behind the step is nearly constant; hence, a free-mixing layer between the injected and the main flows is developed. The distributed pressure rise near the surface leads to formation of oblique shock waves, largely canceling the expansion at the edge of the step. The angle of the forward Mach line can be determined using the Prandtl–Meyer theory for expansion waves occurring when a supersonic flow is turned away from itself. According to this approach, the initial angle of the expansion fan is a function of the incoming flow Mach number only. As it is seen in Fig. 6(c) the numerically computed forward Mach-line angle is in good agreement with the Prandtl–Meyer theory.

As a result of the first film-flow injection, the boundary layer above the second step, shown in Fig. 6(b), is thicker compared to the first one, shown in

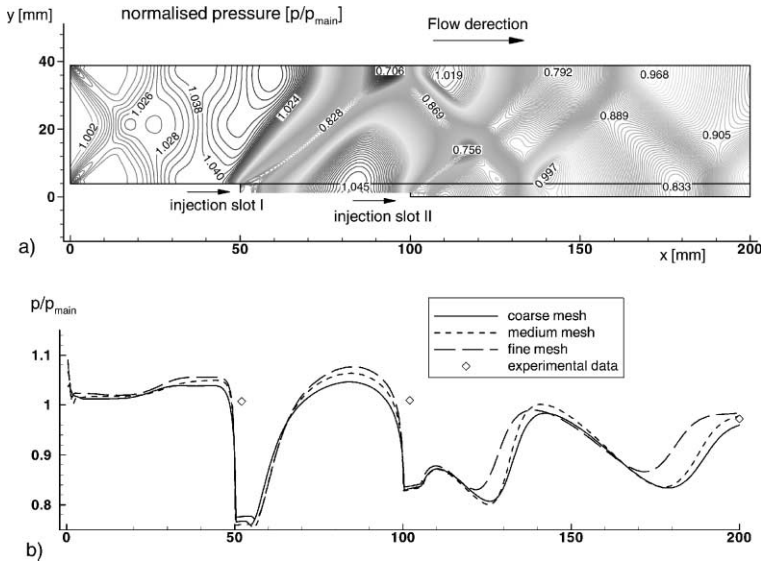

Fig. 5. (a) Pressure contours, fine mesh result ($j_1 = (\rho u)_{\text{slot1}}/(\rho u)_{\text{main}} = 0.07$; $j_2 = (\rho u)_{\text{slot2}}/(\rho u)_{\text{main}} = 0.26$). (b) Pressure distributions along the bottom wall of the channel with coarse, medium and fine mesh results (pressure measurement points are shown in Fig. 1.)

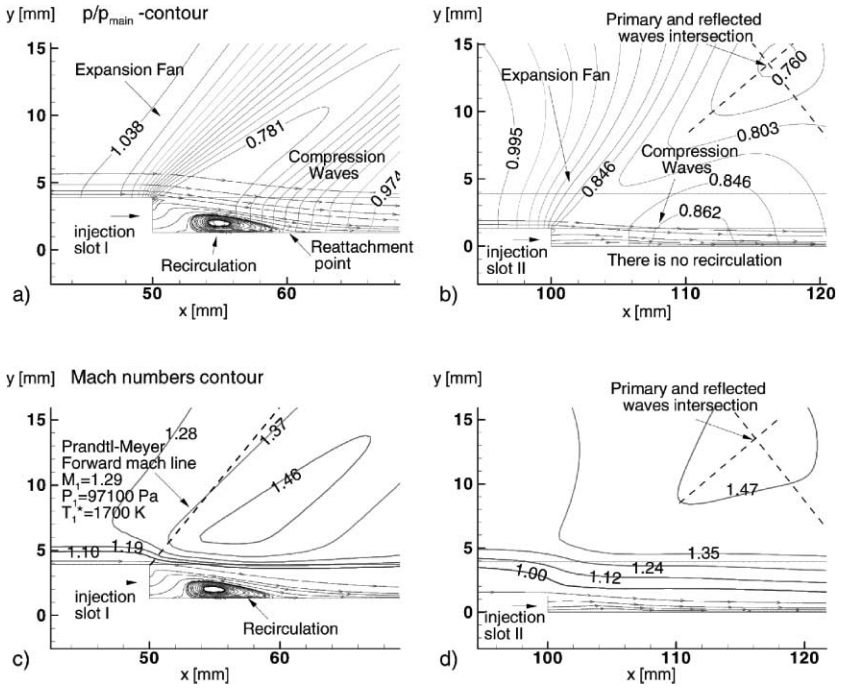

Fig. 6. (a) and (b) pressure contours and streamlines around the first $j_1 = (\rho u)_{\text{slot1}}/(\rho u)_{\text{main}} = 0.07$ and the second $j_2 = (\rho u)_{\text{slot2}}/(\rho u)_{\text{main}} = 0.26$ slots; (c) and (d) Mach contours and streamlines around the first and the second slots, respectively.

Fig. 6(a). The thick subsonic boundary layer leads to less rapid expansion and higher pressure in the near-slot region. Consequently, the main flow only slightly changes its direction and re-compression is relatively small, with no flow recirculation observed.

As depicted in Fig. 5, the computed pressure distributions match the experimental measurements well at the outlet section of the channel, and are under-predicted in the region downstream of the injection points. The pressure measurements are performed immediately

behind the porous injection slots on the centerline of the channel (see Fig. 1). The uncertainty in turbulence modeling for the mixing layer is a possible cause of inaccurate prediction of the expansion and compression characteristics. Such issues are discussed before, such as in [18] for flow over a supersonic projectile after body. However, for the modest supersonic Mach numbers in this case, one does not expect the compressible turbulence effects to be the main source of uncertainties. A very similar wall-pressure behavior downstream of the normal slot injection is also reported in [25]. The original k–ε model along with a version incorporating streamlines curvature modification (which involves the dependence of C_μ on streamlines curvature), and two low-Reynolds number modifications have been tested. Only the curvature-based k–ε model seemed to produce a slight improvement. Similar findings are reported in Ref. [26] while comparing a Reynolds stress model with the original k–ε model on the slot geometry in cross-flow.

3.3. Non-equilibrium model of turbulence

In view of the above observations, the non-equilibrium effects in the k–ε model [19] (realized via the modification of $C_{\varepsilon 1}$ based on the ratio $P/\rho\varepsilon$) have been investigated in this study. In complex fluid flows, such as those with rotation, adverse pressure gradient, recirculation, and large streamline curvature, the assumption of equilibrium between the production and dissipation of turbulent kinetic energy is incorrect. Dynamic characteristics create extra length and time scales according to the local flow structure. However, in the original model, the equilibrium condition is used to assign the model parameters [22].

The coefficient $C_{\varepsilon 1}$, responsible for turbulence production, can be modified and calculated based on current values of production P and dissipation rate ε, so that if the equilibrium condition is met, the coefficient recovers its original value:

$$P_\varepsilon \frac{P}{\rho\varepsilon} = \left[C_{\varepsilon 1}\frac{\varepsilon}{k}P\right]\frac{P}{\rho\varepsilon} \tag{15}$$

The recovering effect of the non-equilibrium model in balancing the turbulence is clearly seen in Fig. 7(a)–(d). In regions of strong non-equilibrium, the dissipation dominates, leading to lower turbulence intensities. Table 5 compares the near-slot pressure between computational and experimental results.

A test case, shown in Fig. 7(e)–(f), is presented to highlight this feature of non-equilibrium model. The production term in the k-equation is artificially increased by a factor of three in five nodes downstream the injection slot, where the free-stream shear layer develops. Consequently, there is a noticeable decrease in turbulence intensity (Fig. 7(f)). Observing the values of static pressure on the wall (Table 5) and the turbulence intensity plots (Fig. 7(b), (d), and (f)) a correspondence between mixing-layer turbulence and momentum/pressure field in the vicinity of injection slot seems obvious.

3.4. Film cooling

The computed wall temperature distribution downstream of the second injection slot is not in close agreement with the experimental data, especially in the near-slot region (Fig. 8). The exact source of the problem is not clear. Observing the adiabatic wall temperature distribution in Fig. 8, the deficiency of Eddy-viscosity model in the near-slot region leads to overestimation of film cooling efficiency, similar to the conclusion reached in Ref. [9]. On the other hand, turbulence overproduction in the free-stream mixing layer seems responsible for uncertainties in pressure estimation. Furthermore, a decrease in turbulence intensity, caused by a higher dissipation rate, results from the non-equilibrium correction in the turbulence model, leads to a worse temperature underestimation (Fig. 8).

From the aforesaid facts follows that one of the source of uncertainty is the turbulent Prandtl number [16], which is not a constant. A value of lower than 1 does not necessarily imply that the temperature profile is wider than the velocity profile but merely that the two shapes are different. It seems that the standard relation between thermal and eddy diffusivities fails in the near-slot region, which leads to underestimation of the normal heat flux component.

3.5. Integral method

To help shed light on the current CFD-based prediction, we have also employed an integral method based on the asymptotic theory of turbulence and semi-empirical correlations [6–8].

3.5.1. Derivation

In the case of tangential film-flow injection there is a small region near the slot where the temperature is approximately unchanged. The length of this region (x_0) is called the effective cooling length and can be estimated according to the theory of turbulent jets [27], based on the assumption that this region is characterized by an approximately constant momentum thickness and a zero heat flux value. The wall layer develops inside the injected flow and is insensitive to the main flow behavior; the wall-jet turbulence dominates and the original law of the wall is not valid in this region. However, it is known from experiments [4] that local disturbances in the momentum field ($x \in [x_{\text{slot}}, x_0]$) do not substantially influence the heat-transfer processes.

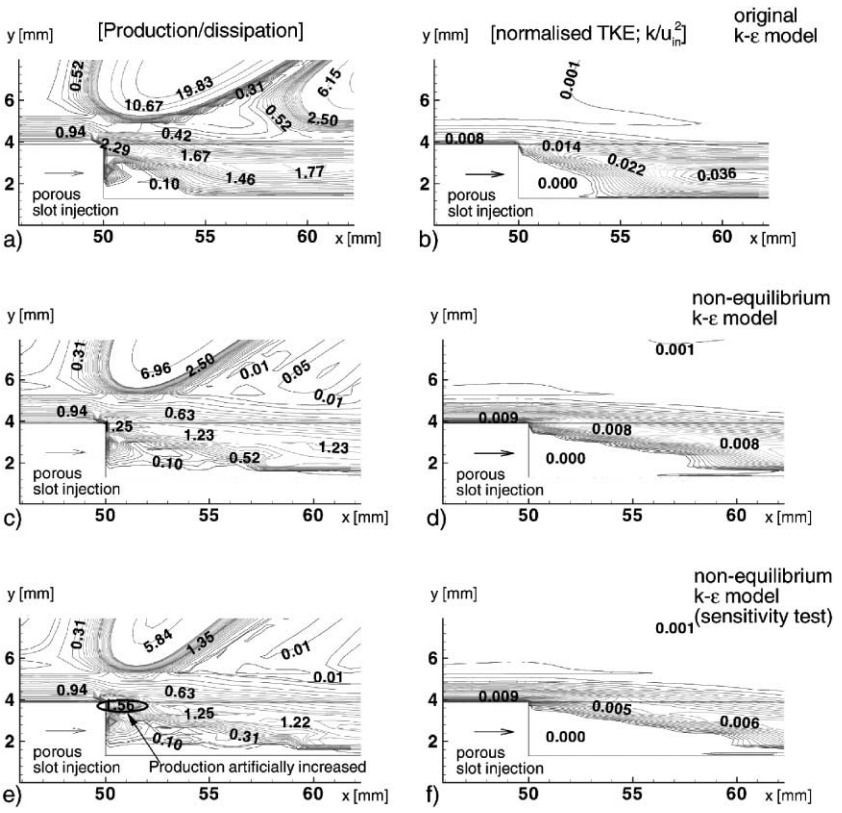

Fig. 7. First slot film-flow injection/mixing-layer turbulence: (a) and (b) original k–ε model result; (c) and (d) non-equilibrium k–ε model result; (e) and (f) non-equilibrium k–ε model with locally increased production (sensitivity test) ($j_1 = (\rho u)_{\text{slot1}}/(\rho u)_{\text{main}} = 0.07$, $T_{\text{slot1}} = 583$ [K]).

Table 5
Effect of non-equilibrium turbulence model parameters on the computed pressure in the near-slot regions. Subscripts "1" and "2" denote the identity of the slot, *main*—parameter at the main flow inlet

Experiment	Original k–ε	$1.44 < C_{\varepsilon 1}(P/\rho\varepsilon) \leqslant 1.44 \times 3$	Test: $P \times 3$ (only five nodes)
p_1/p_{main} 1.009	0.740	0.8370	0.851
p_2/p_{main} 1.020	0.828	0.87	0.881

Downstream of the effective cooling length region ($x > x_0$), where shear-layer turbulence meets the wall, the characteristics of the injected film flow disappear and a turbulent boundary layer develops [2–4].

Performing the integration of the boundary layer equations over the energy boundary layer and using the continuity equation, the resulting equation of energy is obtained [8]:

$$\frac{\mathrm{d}Re_H^{**}}{\mathrm{d}\breve{x}} + Re_H^{**}\left[\frac{1}{u_\infty}\frac{\mathrm{d}u_\infty}{\mathrm{d}\breve{x}} + \frac{1}{(H_\infty - H_{\mathrm{w}})}\frac{\mathrm{d}(H_\infty - H_{\mathrm{w}})}{\mathrm{d}\breve{x}}\right] = \frac{q_{\mathrm{w}}}{c_{p\infty}\rho_\infty u_\infty (H_\infty - H_{\mathrm{w}})} Re_L = StRe_L \tag{16}$$

Here the enthalpy layer-based Reynolds number is determined as follows:

$$Re_H^{**} = \frac{\rho_\infty u_{T\infty}\delta_H^{**}}{\mu_\infty}; \quad \delta_H^{**} = \int_0^\delta \frac{\rho u}{\rho_\infty u_{T\infty}}\left(1 - \frac{H - H_{\mathrm{w}}}{H_\infty - H_{\mathrm{w}}}\right)\mathrm{d}y; \tag{17}$$

The film cooling efficiency definition equation in the case of foreign gas injection (the injection of cooling air into the flow of combustion gases) has the following form [5]:

$$\Theta = \frac{H_\infty - H_{\mathrm{wall}}}{H_\infty - H_{\mathrm{slot}}} = \frac{Re_{H0}^{**}}{Re_H^{**}} \tag{18}$$

where the enthalpy thickness based Reynolds numbers Re_H^{**} and Re_{H0}^{**} can be obtained from the solution of Eq. (16), Re_{H0}^{**} represents the initial energy thickness at the point of injection, tacking into account the prehistory of the flow and the impulse of the injecting flow itself.

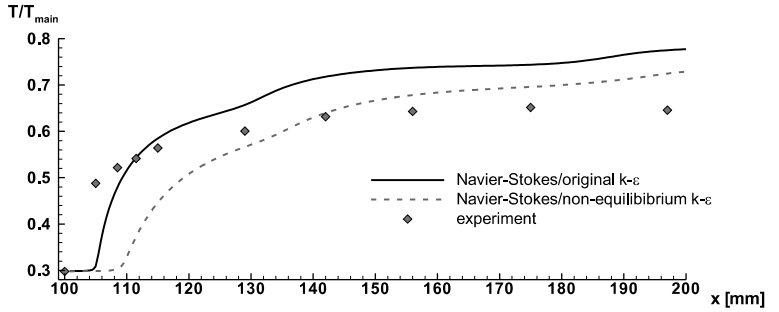

Fig. 8. Wall temperature distribution downstream of the second injection slot: comparison of non-equilibrium and original turbulence models, and experiment. ($j_2 = (\rho u)_{\text{slot2}}/(\rho u)_{\text{main}} = 0.26$, $T_{\text{main}} = 1773$ [K]—main flow stagnation temperature).

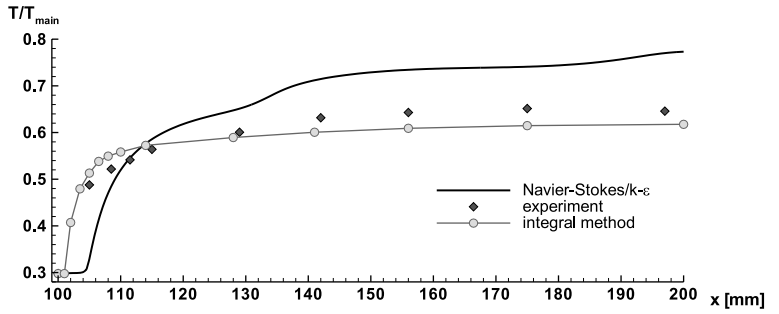

Fig. 9. Comparison of experimental adiabatic wall temperature distribution with numerical and integral method results downstream the second injection slot. ($j_2 = (\rho u)_{\text{slot2}}/(\rho u)_{\text{main}} = 0.26$, $T_{\text{main}} = 1773$ [K]—main flow stagnation temperature).

In the integral method the influence of different perturbation factors on the heat transfer processes is estimated using the parametric expressions as follows:

$$St = St_0 \frac{St}{St_0} = St_0 \Psi = St_0 \Psi_{\text{T}} \Psi_M \Psi_{\text{R}} \cdots = St_0 \prod_{i=1}^{n} \Psi_i \qquad (19)$$

Here, Ψ_{T}, Ψ_{M}, Ψ_{R} are the laws representing the influence of non-isothermal boundary conditions, compressibility of gas flow, wall roughness, and so on. The equations used for estimation of relative laws and detailed discussions are presented in Refs. [5–8]. The Stanton number under the standard conditions (flow on the smooth flat surface) St_0 is estimated using the power law of heat transfer [5] presented below.

$$St_0 = A Re_H^{**-m} Pr^{-0.75} \qquad (20)$$

The coefficients A and m in Eq. (20) are the functions of the momentum thickness based Reynolds number Re^{**}.

3.5.2. Assessment of the integral model

The outcome of Eqs. (16) and (18) is assessed in Fig. 9. It is interesting to note that the present one-parameter integral method provides better accuracy than the Navier–Stokes-based solutions. This technique is partially based on some degrees of empiricism, namely, the Stanton number from Eq. (20) and the exponent in the velocity power law from Eq. (14), and appears to be well correlated for the flow in the present configuration. The Navier–Stokes-based model, aided with the present level of the turbulence closure, is capable of predicting the gross flow features but has deficiency in accounting for mechanisms such as spreading rate and heat transfer in mixing layers.

4. Conclusion

The simulation of supersonic turbulent flow in a rectangular channel with tangential injection of coolant through the porous slots has been conducted. It is shown that the Navier–Stokes model along with the k–ε turbulence model reproduces reasonably well the streamlines near the sectioned wall, and shows that film-flow injection through the steps shifts the shock locations. Numerically computed pressure and adiabatic wall temperature distribution are in less satisfactory agreement to the experimental data. It seems that these predictive deficiencies result from turbulence modeling in the mixing layer. The implementation of the non-equilibrium k–ε model gives some improvement in computing the momentum equations, but fails to improve the

prediction of heat transfer downstream the injection points.

The integral method is shown to be capable of accounting for the wall temperature profile under the given flow condition and geometry. Clearly, there is room to refine the Navier–Stokes model, which can benefit from the insight gained from the integral and experimental approaches.

References

[1] R.J. Goldstein, Film cooling heat transfer, in: T.F. Irvine Jr., J.P. Hartnett (Eds.), Advances in Heat Transfer, vol. 7, Academic press, New York, 1971, pp. 321–379.

[2] S.K. Kacer, J.H. Whitelaw, Some properties of near-wall plate turbulent jet in moving flow, J. Appl. Mech. 35 (N4) (1968) 19–30.

[3] A.B. Lebedev, U.Y. Shvaikovsky, Experimental investigation of velocity and turbulence in the film flow, TVT 3 (N4) (1965) 569–576.

[4] R. Seban, L. Beck, Temperature and velocity profiles in turbulent boundary layer with tangential slot film-flow injection, Heat-Transfer (N7) (1962) 58–59.

[5] S.S. Kutateladze, A.I. Leont'ev, Turbulent Boundary Layers in Compressible Gases, translated by D.B. Spalding, Academic Press, New York, 1964.

[6] S.S. Kutateladze, A.I. Leont'ev, Film cooling in turbulent boundary layers, TVT 1 (N2) (1963) 281–290.

[7] M.I. Osipov, A.I. Leont'ev, et al., in: Engineering Thermo-Physical Problems of Low Temperature Plasma in Encyclopedia of Low Temperature Plasma, vol. 4, 2000, pp. 460–505.

[8] A.I. Leont'ev, M.I. Osipov, et al., Low Temperature Plasma Plasmatrone Walls' Heat Protection, Institute of Thermophysics, Novosibirk, 1995, vol. 12, p. 98.

[9] A.H. Lefebvre, Gas Turbine Combustion, Hemisphere, Washington, DC, 1983.

[10] S.S. Thakur, J.A. Wright, W. Shyy, Convective film cooling over a representative turbine blade leading-edge, Int. J. Heat Mass Transfer 42 (1999) 2269–2285.

[11] M.I. Osipov, Heat protection in flow ducts of high temperature power plants, in: Proceedings of International Conferrence: Advanced Technologies at the Threshold of XXI Century, ICAT'98, Moscow, vol. 2, 1998, pp. 255–257.

[12] M.I. Osipov, Conjugate Heat Transfer on the walls with porous and tangential porous sectional injection, in: Prop. of XI All Russia Conference: Gas Turbine and Combined Plants and Engines, Moscow, 2000, p. 60.

[13] M.J. Kenworthy, J.A. Schetz, An Experimental Study of Slot Injection into a Supersonic Stream, Aerospace Engineering Department, Virginia Polytechnical Institute and State University, Blacksburg, January 1973, p. 41, Report: NASA-CR-2128.

[14] V. Zakkay, C.R. Wang, Skin Friction Reduction by Slot Injection at Mach 0.8, New York University, Westbury, Aerospace and Energetic Laboratory, 31 July 1975, p. 85, Report: NASA-CR-146355.

[15] C.D. Whitcomb, Compressible Turbulence Measurements in the Mixing Layer of an Adiabatic Normal Slot Injection into Supersonic Flow, Air Force Institute of Technology, Write-Patterson AFB, OH, School of Engineering, December 1995, p. 86, Report: AFIT/GAE/ENY/95D-24.

[16] T. Cebeci, P. Bradshaw, Physical and Computational aspects of Convective Heat Transfer, Springer-Verlag, New York, 1984.

[17] D.C. Wilcox, Turbulence Modeling for CFD, second ed., DCW Industries, 2000, p. 243.

[18] W. Shyy, V.S. Krishnamutry, Compressibility effects in modeling complex turbulent flows, Prog. Aerospace Sci. 33 (1997) 587–645.

[19] W. Shyy, S.S. Thakur, H. Ouyang, J. Liu, E. Blosch, Computational Techniques for Complex Transport Phenomena, Cambridge University Press, Cambridge, 1997.

[20] W. Shyy, Computational Modeling for Fluid Flow and Interfacial Transport, Elsevier, Amsterdam, The Netherlands, 1994.

[21] S. Thakur, W. Shyy, Some implementation issues of convection schemes for finite-volume formulations, Numer. Heat Transfer, Part B 24 (1993) 31–35.

[22] B.E. Launder, D.B. Spalding, The numerical computation of turbulent flows, Comp. Meth. Appl. Mech. Eng. 3 (1974) 269–289.

[23] S.V. Patankar, Numerical Heat Transfer and Fluid Flow, Hemisphere, Taylor&Francis, Washington, DC, 1980.

[25] P.G. Kassimatis, G.C. Bergeles, T.V. Jones, J.W. Chew, Numerical investigation of the aerodynamics of near-slot film cooling, Int. J. Numer. Meth. Fluids 32 (2000) 97–117.

[26] J. Alvares, W.P. Jones, R. Seoud, Predictions of momentum and scalar fields in a jet in cross flow using first and second order turbulence closures, AGARD CP-534, Computational and Experimental Assessment of Jets in Cross Flow, 1993.

[27] G.N. Abramovich, The Theory of Turbulent Jets, MIT, Cambridge, MA, 1963.